Supplementary Information for 'Increasing risks of extreme salt intrusion events across European estuaries in a warming climate'

Jiyong Lee[1*], Bouke Biemond[1], Huib de Swart[1] and Henk A. Dijkstra[1]

[1]Institute for Marine and Atmospheric research Utrecht (IMAU), Utrecht University, Princetonplein 5, Utrecht, 3584 CC, the Netherlands.

*Corresponding author(s). E-mail(s): j.lee3@uu.nl;
Contributing authors: w.t.biemond@uu.nl; h.e.deswart@uu.nl; h.a.dijkstra@uu.nl;

This document contains:
- Supplementary Note S1-S2;
- Supplementary Table S1-S2;
- Supplementary Figure S1-S6.

Note S1 Bias correction for the modeled river discharge in CESM-LE2

In global climate model results, systematic over- or under-estimation are often shown as compared to observations due to complex earth system processes that could not be fully resolved or properly parameterized. Quantile Delta Mapping (QDM) is one of the bias adjustment methods to avoid such systematic errors in future projections of climate variables. The main idea of QDM is mapping each quantile of climate variables in simulations to that of observational data during the historical period while preserving its trends (or difference) in the future. Initially developed for precipitation, QDM has been widely used for many other climate variables, since projected future simulations using QDM are shown to preserve their quantile characteristics (e.g. the 95th percentile) and return periods [1]. We use QDM [1] to adjust systematic biases in the modeled river discharge in CESM-LE2. In [2], comprehensive descriptions of QDM and its recent advancements are provided.

Supplementary Fig. S2 illustrates how QDM for the modeled river discharge is implemented in this study. As shown in Fig. S2a, two time periods are determined in the modeled river discharge timeseries: historical $Q_{m:h}$ (observation time in Supplementary Table S1) and projection $Q_{m:p}$ (1996-2100). Here, the first letter in the subscript m and o indicate model and observation results. The second letter h and p denote historical and projection time periods, respectively. For the modeled river discharge at certain time t in the projection period $Q_{m:p}(t)$ (red circle in Fig. S2a), time-dependent CDFs are created with a time window of W^{bc}=35 yrs, that is $G_{m:p}(t)$ (orange solid line in Fig. S2c). Next, we obtain the quantile τ that corresponds to $Q_{m:p}(t)$ in $G_{m:p}(t)$ and the representative modeled river discharge that is associated with τ in the historical period $G^{-1}_{m:h}(\tau)$ using the ensemble averaged CDF (gray dashed line in Fig. S2c). The relative statistical difference between the historical and projection periods is calculated in the modeled river discharge at the quantile τ:

$$\delta = \frac{Q_{m:p}(t)}{G^{-1}_{m:h}(\tau)} = \frac{G^{-1}_{m:p}(\tau)}{G^{-1}_{m:h}(\tau)}. \tag{S1}$$

Thereafter, the relative statistical difference δ is mapped on the CDF of the observed river discharge at the quantile τ, that is $G^{-1}_{o:h}(\tau)$ in Fig. S2d. The bias corrected river discharge at the time t in the projection period is now expressed as:

$$Q^{bc}_{m:p}(t) = \delta G^{-1}_{o:h}(\tau). \tag{S2}$$

The bias correction is implemented for every t in the projection period of the modeled river discharge. At the beginning and the end of the period, $t \leq \frac{W^{bc}-1}{2}$ or $t \geq 2100 - \frac{W^{bc}-1}{2}$, the first and the last 35 yrs are used to generate the time-dependent CDF in the projection period $G_{m:p}(t)$. Note that we use individual ensemble timeseries in the projection period, but ensemble averaged CDF is employed for the historical period. That is because ensemble variability in the climate models is significantly suppressed if individual ensemble timeseries are used for both historical and projection periods. It is ensured that the CDF of the observed river discharge is statistically converged for each river basin. We performed tests with different lengths of the time window (varied from 30 yrs to 40 yrs), but they had negligible effects on the bias-corrected river discharge.

Note S2 Mixing parameterization for the salt intrusion length model

The mixing processes in Eq. 1 (main text) are parameterized by the following constants under the partial slip condition [3] (note that the no-slip condition is used in [4]):

$$C_0 = K_h \ [\mathrm{m}^2/\mathrm{s}], \tag{S3a}$$

$$C_1 = 0.00305\frac{H^2}{K_v} \ [\mathrm{s}], \tag{S3b}$$

$$C_2 = (0.0275)^2\frac{c^2H^4}{A_vK_v} \ [\mathrm{m}^2], \tag{S3c}$$

$$C_3 = (0.0365)^3\frac{c^4H^6}{A_v^2K_v} \ [\mathrm{m}^4/\mathrm{s}]. \tag{S3d}$$

In Eqs. S3, K_h [m^2/s] is the horizontal eddy diffusivity; K_v [m^2/s] and A_v [m^2/s] are the vertical eddy diffusivity and viscosity; H [m] is the water depth at the mouth of an estuary; $\beta = 7.6 \times 10^{-4}$ [$-$] is the saline contraction coefficient; $s_{ocn} = 35$ [psu] is the prescribed salinity at the open ocean; $g = 9.81$ [m/s^2] is the gravitational acceleration and $c = \sqrt{g\beta s_{ocn}H}$. The eddy mixing are parameterized as:

$$K_h = \epsilon\frac{L_tU_T}{\pi}(1 - \sqrt{\frac{2B}{\pi L_t}}), \tag{S4a}$$

$$A_v = c_vU_TH, \tag{S4b}$$

$$K_v = A_v/Sc. \tag{S4c}$$

Here, U_T is the tidal current amplitude, $L_t = \frac{U_TT_T}{\pi}$ is the tidal excursion length induced by the M2 constitute and $T_T = 12.42$ hrs is the M2 tide frequency. Furthermore, $\epsilon = 0.1$ is an empirical constant [5], $c_v = 0.86\times10^{-4} - 1.56\times10^{-4}$ is a tuning coefficient, B is the estuary width, and $Sc = 2.2$ is the Schmidt number [6]. The geometries of estuaries, the tidal current amplitudes, and the corresponding mixing parameters are summarized in supplementary Table S2. The model calculates the time-averaged salt intrusion length during the observation time period with a 100 m margin of error compared to the reported values in the literature, that is $\mid \overline{X_{2,mod}} - \overline{X_{2,obs}} \mid \leq 100$ m.

Table S1 River discharge observation data used in this study. The rows are in the order of ascending latitude.

Estuary	Station	Country	Observation time	Location (lon, lat)
Guadalquivir	Alcalá del Rio dam	Spain	1931/07/01 - 2011/04/28	(-5.98, 37.52)
Douro	Carrascal	Spain	1967/01/01 - 1989/12/31	(-5.81, 41.49)
Maritsa	Svilengrad	Bulgaria	1978/01/01 - 1986/12/30	(26.2, 41.77)
Ebro	Zaragoza	Spain	1944/01/01 - 2016/12/31	(-0.88, 41.66)
Rhone	Beaucaire	France	1969/01/01 - 1979/12/30	(4.67, 43.92)
Gironde	Lamonzie-Saint-Martin Tonneins	France	2009/01/01 - 2020/12/31	(0.35, 44.85) (0.30, 44.39)
Danube	Ceatal Izmail	Romania	1931/01/01 - 2010/12/30	(28.72, 45.22)
Loire	Montjean	France	1971/01/01 - 1979/12/30	(-0.83, 47.38)
Dnieper	Dnepr Power Plant	Ukraine	1955/01/01 - 1984/12/30	(35.15, 47.92)
Don	Razdorskaya	Russia	1952/01/01 - 2010/12/30	(40.65, 47.54)
Tamar	Gunnislake	UK	1957/01/01 - 2020/12/31	(-4.22, 50.53)
Scheldt	Schelle calc	Belgium	1971/01/03 - 2022/11/02	(4.32, 51.13)
Thames	Kingston	UK	1931/01/01 - 2019/12/31	(-0.31, 51.42)
Rhine-Meuse	Lobith Venlo	Netherlands	1997/01/01 - 2019/12/30	(6.11, 51.84) (6.16, 51.37)
Oder	Hohensaaten-Finow	Germany	1931/01/01 - 2019/12/30	(14.14, 52.87)
Elbe	Neu Darchau	Germany	1931/01/01 - 2019/12/31	(10.89, 53.23)
Humber	Colwick Skelton Buttercrambe Kildwick Bridge	UK	1974/01/01 - 2009/12/31	(-1.08, 52.95) (-1.13, 53.99) (-0.89, 54.02) (-1.98, 53.91)
Nemunas	Kauno Hps	Lithuania	1980/01/01 - 2003/12/30	(23.98, 54.88)
Gota	Vargoens Krv	Sweden	1940/01/01 - 2020/12/30	(12.37, 58.36)
Glomma	Langnes	Norway	1931/01/01 - 2018/12/30	(11.12, 59.61)
Angermanalven	Solleftea Krv	Sweden	1931/01/01 - 2020/12/30	(17.27, 63.17)
Onega	Porog	Russia	1945/01/01 - 2003/12/31	(38.47, 63.82)

Table S2 Geometries of estuaries and tidal current amplitude used for the mixing parameterization in the time-dependent salt intrusion model. Here, B is the estuary width; H is the water depth; U_T is the tidal velocity; A_v is the vertical viscosity; K_v and K_h are the vertical and horizontal eddy diffusivity. The saltwater intrusion length ranges are the reported values in the corresponding references.

Estuary	Saltwater intrusion length range [km]	B [m]	H [m]	U_T [m/s]	A_v [m^2/s] $\times 10^{-4}$	K_v [m^2/s] $\times 10^{-4}$	K_h [m^2/s]	References
Guadalquivir	54.9 - 59.1	500	7.1	1.15	7.48 ± 2.68	3.40 ± 1.22	521 ± 37	[7]
Gironde	32 - 80	5000	10	1	8.74 ± 1.11	3.97 ± 0.51	245 ± 21	[8]
Tamar	17 - 27	500	3	0.7	1.93 ± 0.22	0.88 ± 0.10	165 ± 1	[9, 10]
Scheldt	58 - 120	4200	10	0.85	10.70 ± 1.44	4.85 ± 0.66	169 ± 13	[11]
Thames	38 - 76	2070	7	0.9	6.69 ± 1.36	3.04 ± 0.62	234 ± 11	[12]
Rhine-Meuse	35	600	15	0.85	12.5 ± 1.39	5.68 ± 0.63	271 ± 23	[13]
Elbe	49 - 94	3500	10	1	5.49 ± 0.58	2.50 ± 0.26	265 ± 24	[14]
Humber	30 - 95	6000	8	1	9.71 ± 1.30	4.41 ± 0.59	201 ± 7	[15, 16]

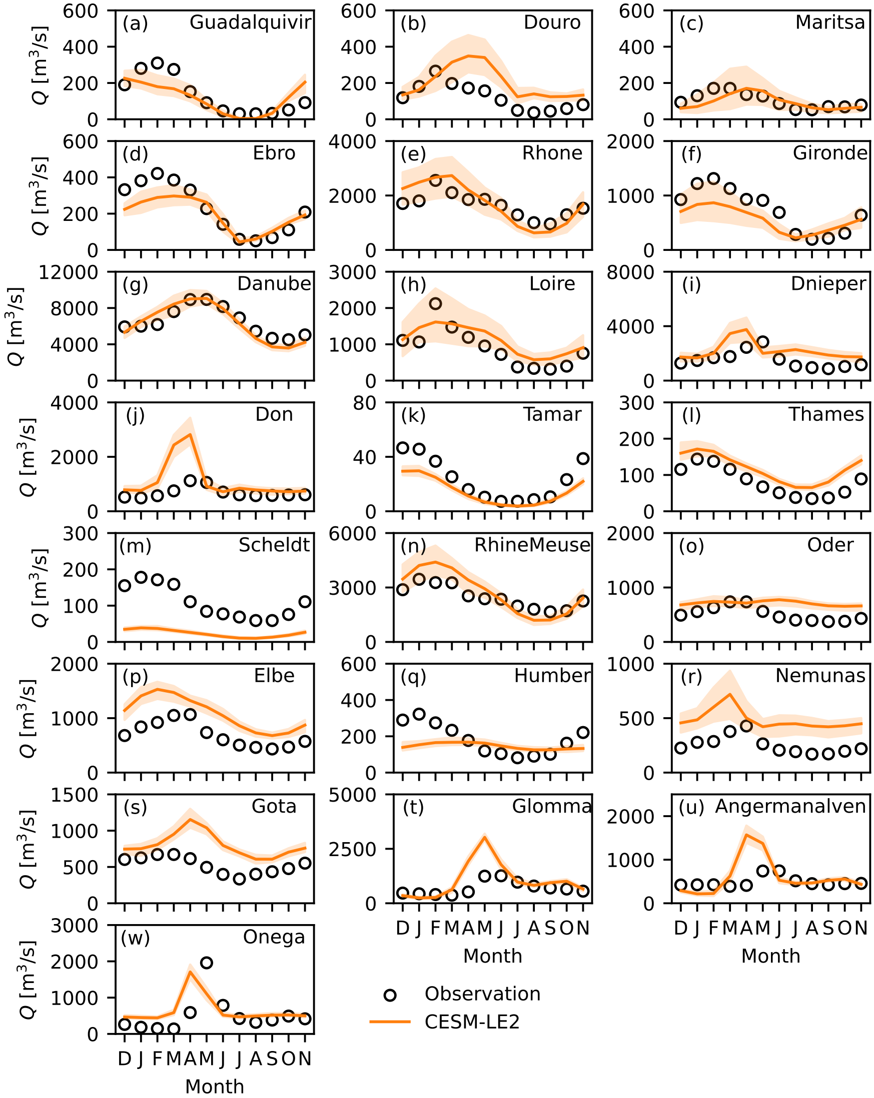

Fig. S1 Seasonal averaged freshwater discharge at the outlet of the selected river basins.

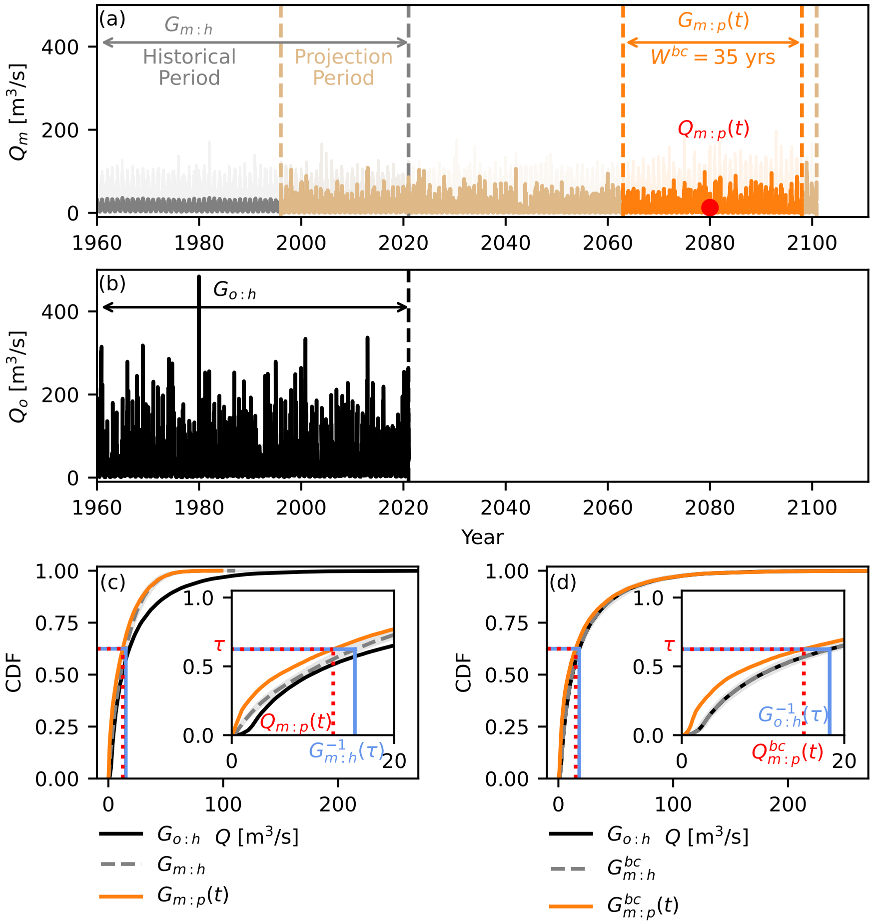

Fig. S2 An example of bias correction for the Tamar river basin. (a) Timeseries of the modeled river discharge in CESM-LE2. Here, the solid lines in the historical and projection periods indicate ensemble-averaged and individual ensemble timeseries, respectively. The shaded areas show the ensemble maximum and minimum. The red dot, $Q_{m:p}(t)$, is the modeled river discharge at certain time t in the projection period. The horizontal orange arrow, W^{bc}, shows a length of the bias correction window to create time-dependent CDF, $G_{m:p}(t)$, in the projection period that corresponds to $Q_{m:p}(t)$. (b) Timeseries of the observed river discharge. CDFs (c) before and (d) after QDM. In the panels, the first letter in the subscript m and o are associated with model and observation. The second letter in the subscript h and p denote historical and projection periods. The superscript bc indicates the bias correction.

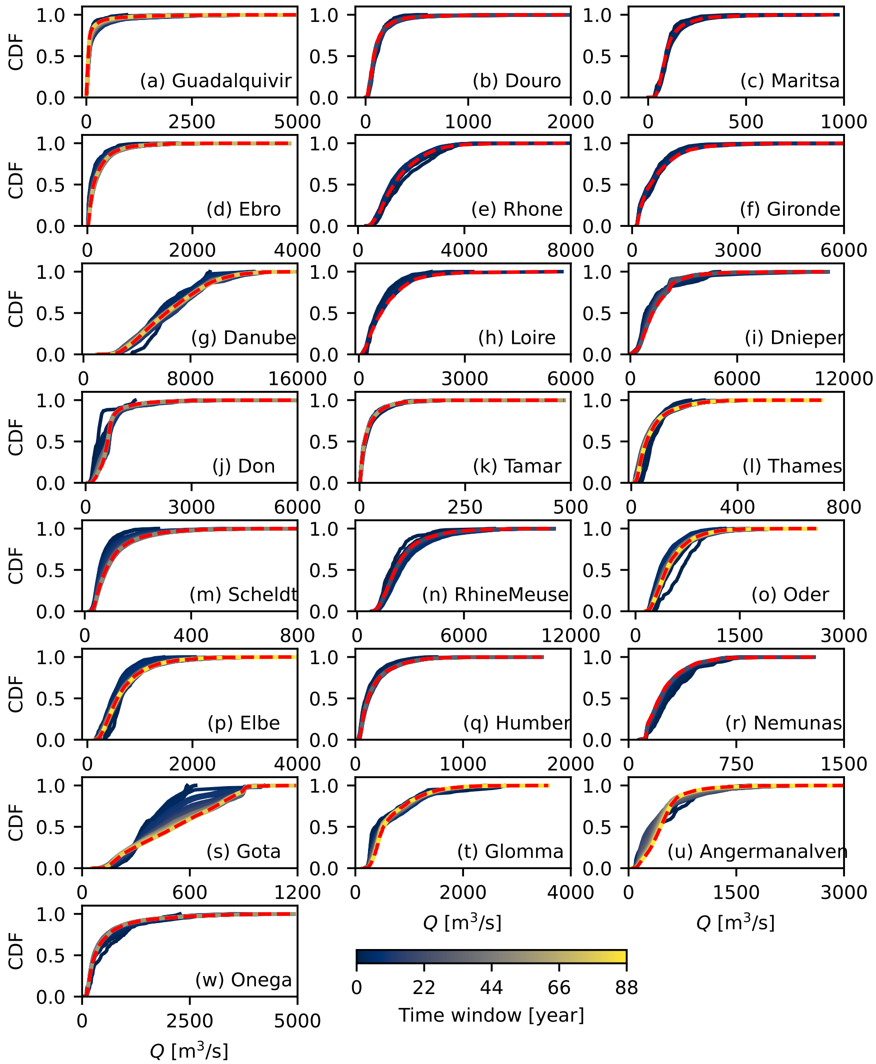

Fig. S3 Convergence of cumulative distribution functions in the river discharge observation under varying time windows. Here, the time window is the varying length of periods from the starting date of the observation. The red dashed lines are the resulting CDFs when the entire observation time periods are considered, which is summarized in Table S1.

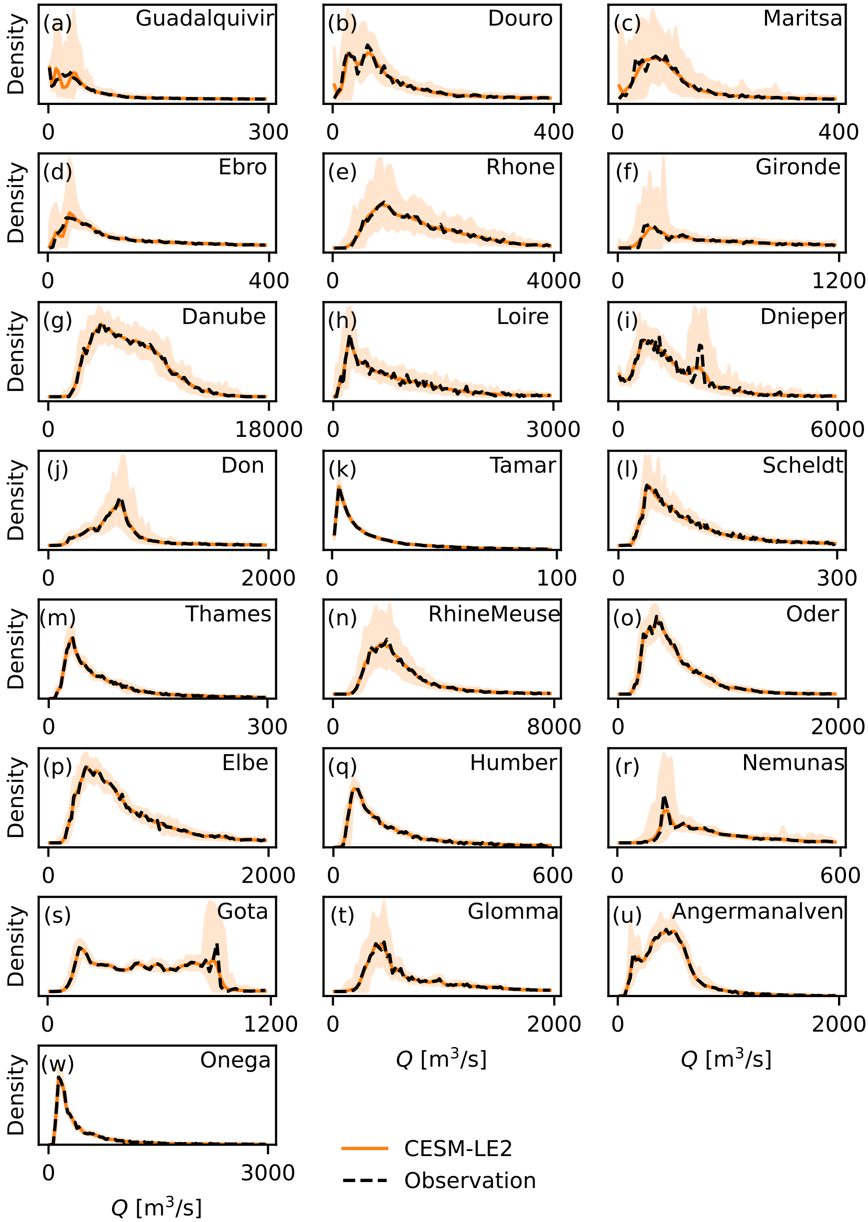

Fig. S4 Probability density comparing the bias-corrected river discharge and the observed river discharge. Note that a range of river discharge in the horizontal axis in the PDFs excludes low probability regions for the visualization. The entire ranges of freshwater discharge for each river basin are given in Fig. S3.

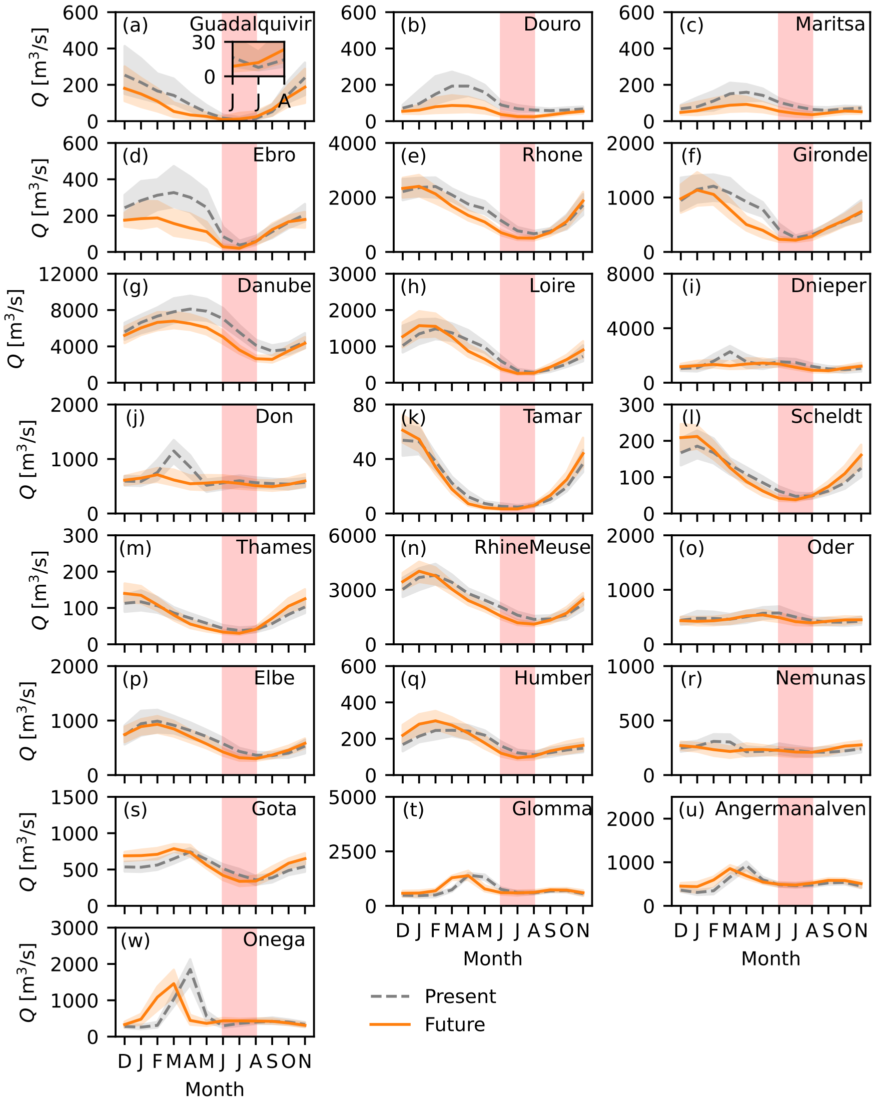

Fig. S5 Changes in the seasonal average of the bias-corrected river discharge between present (1996-2030) and future (2066-2100) periods under the SSP 3-7.0 scenario in CESM-LE2. Here, the vertical red-shaded areas show the summer months.

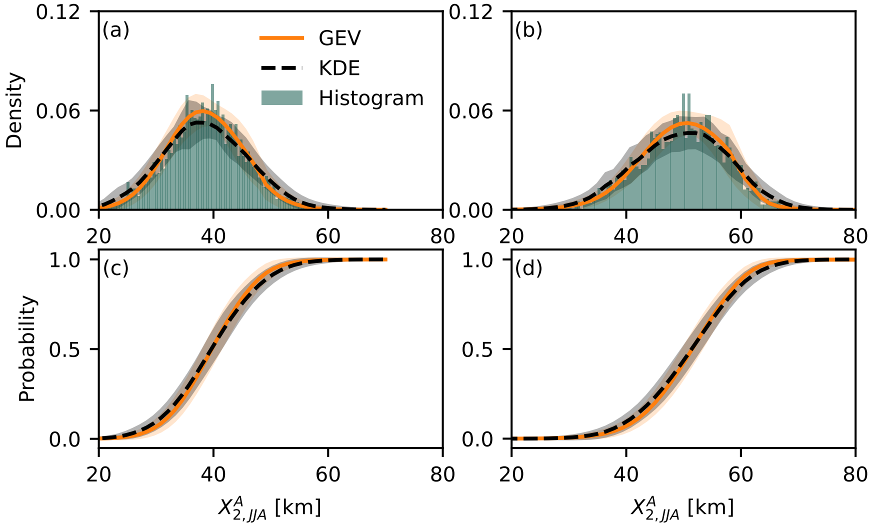

Fig. S6 A comparison of the modeled annual mean summer month saltwater intrusion length between the fitted GEV, KDE, and histogram in the Tamar Estuary: (a) and (b) are the probability density for the present (1996-2030) and the future (2066-2100) time. (c) and (d) are the same as (a) and (b), but for the probability.

References

[1] Cannon, A.J., Sobie, S.R., Murdock, T.Q.: Bias correction of GCM precipitation by quantile mapping: how well do methods preserve changes in quantiles and extremes? Journal of Climate **28**(17), 6938–6959 (2015). https://doi.org/10.1175/JCLI-D-14-00754.1

[2] Lange, S.: Trend-preserving bias adjustment and statistical downscaling with ISIMIP3BASD (v1.0). Geoscientific Model Development **12**(7), 3055–3070 (2019). https://doi.org/10.5194/gmd-12-3055-2019

[3] Biemond, B., de Swart, H.E., Dijkstra, H.A., Dìez-Minguito, M., *et al.*: Estuarine salinity response to freshwater pulses. Journal of Geophysical Research: Oceans **127**(11), 1–18 (2022). https://doi.org/10.1029/2022JC018669

[4] Chen, S.-N.: Asymmetric estuarine responses to changes in river forcing: A consequence of nonlinear salt flux. Journal of Physical Oceanography **45**(11), 2836–2847 (2015). https://doi.org/10.1175/JPO-D-15-0085.1

[5] MacCready, P.: Estuarine adjustment. Journal of Physical Oceanography **37**(8), 2133–2145 (2007). https://doi.org/10.1175/JPO3082.1

[6] Ralston, D.K., Geyer, W.R., Lerczak, J.A.: Subtidal salinity and velocity in the hudson river estuary: Observations and modeling. Journal of Physical Oceanography **38**(4), 753–770 (2008). https://doi.org/10.1175/2007JPO3808.1

[7] Díez-Minguito, M., Contreras, E., Polo, M., Losada, M.: Spatio-temporal distribution, along-channel transport, and post-riverflood recovery of salinity in the Guadalquivir Estuary (SW Spain). Journal of Geophysical Research: Oceans **118**(5), 2267–2278 (2013). https://doi.org/10.1002/jgrc.20172

[8] van Maanen, B., Sottolichio, A.: Hydro-and sediment dynamics in the Gironde Estuary (France): Sensitivity to seasonal variations in river inflow and sea level rise. Continental Shelf Research **165**, 37–50 (2018). https://doi.org/10.1016/j.csr.2018.06.001

[9] Uncles, R., Stephens, J.: The freshwater-saltwater interface and its relationship to the turbidity maximum in the Tamar Estuary, United Kingdom. Estuaries **16**, 126–141 (1993). https://doi.org/10.2307/1352770

[10] Friedrichs, C.T., Aubrey, D.G.: Tidal propagation in strongly convergent channels. Journal of Geophysical Research: Oceans **99**(C2), 3321–3336 (1994). https://doi.org/10.1029/93JC03219

[11] Naithani, J., de Brye, B., Buyze, E., Vyverman, W., Legat, V., Deleersnijder, E.: An ecological model for the Scheldt Estuary and tidal rivers ecosystem: spatial and temporal variability of plankton. Hydrobiologia **775**, 51–67 (2016). https://doi.org/10.1007/s10750-016-2710-1

[12] Prandle, D.: Saline intrusion in partially mixed estuaries. Estuarine, Coastal and Shelf Science **59**(3), 385–397 (2004). https://doi.org/10.1016/j.ecss.2003.10.001

[13] Van Der Burgh, I.P.: Prediction of the extent of saltwater intrusion into estuaries and seas. Journal of Hydraulic Research **6**(4), 267–288 (1968). https://doi.org/10.1080/00221686809500241

[14] Gisen, J., Savenije, H., Nijzink, R.: Revised predictive equations for salt intrusion modelling in estuaries. Hydrology and Earth System Sciences **19**(6), 2791–2803 (2015). https://doi.org/10.5194/hess-19-2791-2015

[15] Cave, R.R., Ledoux, L., Turner, K., Jickells, T., Andrews, J., Davies, H.: The Humber catchment and its coastal area: from UK to European perspectives. Science of the Total Environment **314**, 31–52 (2003). https://doi.org/10.1016/S0048-9697(03)00093-7

[16] Robins, P.E., Lewis, M.J., Freer, J., Cooper, D.M., Skinner, C.J., Coulthard, T.J.: Improving estuary models by reducing uncertainties associated with river flows. Estuarine, Coastal and Shelf Science **207**, 63–73 (2018). https://doi.org/10.1016/j.ecss.2018.02.015